RSC Advances

PAPER

View Article Online
View Journal | View Issue

Cite this: *RSC Adv.*, 2023, **13**, 28097

Surface modulation for highly efficient and stable perovskite solar cells†

Dongliang Bai,‡[a] Dexu Zheng,‡[c] Shaoan Yang,‡[b] Fengyang Yu,*[b] Xuejie Zhu,[a] Lei Peng,[c] Likun Wang,[b] Jishuang Liu,[c] Dong Yang*[b] and Shengzhong (Frank) Liu *[ab]

Received 7th February 2023
Accepted 16th March 2023

DOI: 10.1039/d3ra00809f

rsc.li/rsc-advances

Defects formed by halide ion escape and wettability of the perovskite absorber are essential limiting factors in achieving high performance of perovskite solar cells (PSCs). Herein, a series of ionic organic modulators are designed to contain halide anions to prevent defect formation and improve the surface tension of the perovskite absorber. It was found that the surface modulator containing Br anions is the most effective one due to its capability in bonding with the undercoordinated Pb^{2+} ions to reduce charge recombination. Moreover, this surface modulator effectively creates a suitable energy level between the perovskite and hole transport layer to promote carrier transfer. In addition, the surface modulator forms a chemisorbed capping layer on the perovskite surface to improve its hydrophobicity. As a result, the efficiency of PSCs based on surface modulators containing Br anion enhances to 23.32% from 21.08% of the control device. The efficiency of unencapsulated PSCs with a surface modulator retains 75.42% of its initial value under about 35% humidity stored in the air for 28 days, while the control device only maintained 44.49% of its initial efficiency. The excellent stability originates from the hydrophobic perovskite surface after capping the surface modulator.

Introduction

In recent years, perovskite solar cells (PSCs) have attracted much attention in the photovoltaic research community due to their remarkable optoelectronic properties such as long carrier diffusion lengths, direct tunable bandgap, high absorption coefficients, and extremely low exciton binding energy.[1–3] The power conversion efficiency (PCE) of PSCs has rapidly enhanced to 25.7% since their first demonstration in 2009.[4,5] The photoelectric properties of the charge transport layer and perovskite absorber are the key influencing factors in the high performance of PSCs according to previous reports.[6,7] There are numerous studies focused on charge transport layer such as novel materials, modification, and passivation to successfully improve the efficiency and stability of perovskite devices.[8–13] For the perovskite absorber, its properties including surface roughness, crystallinity, grain size, and defects limit the performance of PSCs.[14–18] Among these restraining factors, the bulk and interface defects of perovskite absorbers particularly impact the charge transfer dynamic of perovskite devices.

Defects are divided into shallow-level defects and deep-level defects. The charges captured by the shallow-level defects will return to the conduction band/valence band and then be collected by the electrode. Therefore, these shallow-level defects have little influence on carrier recombination. However, the charges trapped by the deep-level defects will inevitably suffer non-radiative recombination, and it has a great effect on charge transfer in PSCs.[19,20] In general, deep-level defects are mainly located at grain boundaries and the interface with a high formation energy,[21,22] and the density of deep defects at the perovskite surface is around two orders of magnitude higher than that of the bulk.[23] The surface defects thus dominate the carrier recombination in PSCs. Therefore, effective surface modification to reduce the defects is essential for improving the performance of PSCs.[24,25] To date, post-treatment by coating passivation agents, including Lewis acid-base, alkyl ammonium halide, and organic molecules on the perovskite surface are considered efficient methods to decrease the surface defects. Shi *et al.*[26] added 6,6′-dithiodinicotinic acid and urea as the additives, and the PCE improved from 16.76 to 20.64%. Wang *et al.*[27] introduced thiourea (Lewis acid-base) into the $CH_3NH_3PbI_3$ precursor, the photoelectric performance of the perovskite layer improved, and optimized efficiency was up to 19.80%. Ye *et al.*[28] compared the passivation capacity of three structurally similar alkyl ammonium salts and found that the

[a]*Key Laboratory of Applied Surface and Colloid Chemistry, Ministry of Education, Shaanxi Key Laboratory for Advanced Energy Devices, Shaanxi Engineering Lab for Advanced Energy Technology, School of Materials Science and Engineering, Shaanxi Normal University, Xi'an, 710119, China*

[b]*Dalian National Laboratory for Clean Energy, Dalian Institute of Chemical Physics, Chinese Academy of Sciences, Dalian, 116023, China. E-mail: yufengyang@dicp.ac.cn; dongyang@dicp.ac.cn; szliu@dicp.ac.cn*

[c]*China National Nuclear Power Co., Ltd., Beijing 100097, China*

† Electronic supplementary information (ESI) available. See DOI: https://doi.org/10.1039/d3ra00809f

‡ These three authors contributed equally to this study and share the first authorship.

water contact angle gradually increased when increasing the number of carbon atoms in the alkane. The PCE was enhanced to 21.22% with a great improvement in humidity stability. Hu *et al.*[29] employed organic molecule 4-(aminomethyl) benzoic acid hydroiodide as an organic cation in the $CH_3NH_3PbI_3$ precursor solution. The device showed good stability, and the PCE increased to 15.6%. **Rakita** *et al.*[30] used alcoholic solutions of alkyl ammonium or halides monovalent alkali metal to treat metal (Pb or Sn) films. In this way, halide perovskite films had been formed without the use of toxic Pb^{2+} solutions. Cheng *et al.*[31] employed pyridine-terminated conjugated small organic molecules to link the NiO_x and perovskite layers, and the efficiency improved from 12.53% to 17.00%.

In addition, the capping layer above the perovskite absorber effectively inhibits ion migration and diffusion at the surface and efficiently protects the perovskite degradation from the influence of water and oxygen in the atmosphere. Zhong *et al.*[32] added a polymer mixture of polyvinylpyrrolidone (PVP) and polyethylene glycol into the PbI_2 precursor solution, and there was an efficiency enhancement of 30% over the pristine one. Polymer mixture-modified PSC also represents better air stability. Sandoval-Torrientes *et al.*[33] used a variety of chemically modified fullerenes to prepare perovskite/fullerene blends, and the PCE of ETL-free perovskite devices improved to 14.3%. Chen *et al.*[34] prepare 2D PEA_2PbI_4 capping layers on top of a 3D perovskite film, and a high efficiency of 18.51% with drastically improved stability was obtained.

In this study, we developed an ionic organic modulator, 1-hexadecyl-3-methylimidazolium hexafluorophosphate (1-h-3-MIHFP), 1-hexadecyl-3-methylimidazolium chloride (1-h-3-MICl) and 1-hexadecyl-3-methylimidazolium bromide (1-h-3-MIBr) as the surface modulator layers and compared their effect on the performance of PSCs. Experimental results revealed that all these surface modulator layers effectively enhanced the carrier lifetime and reduced the surface defects of the perovskite absorber. The perovskite devices with 1-h-3-MIBr exhibited the best performance. The efficiency of PSCs based on 1-h-3-MIBr increased to 23.32% from 21.08% of the control device. Meanwhile, the long-term environmental stability of the device based on 1-h-3-MIBr is better than that of the control perovskite device. The efficiency of the unencapsulated perovskite device with 1-h-3-MIBr was maintained at 75.42% of its initial value under about 35% humidity stored in the air for 28 days, while the control device only retained 44.49% of its initial efficiency. The excellent stability contributed to the hydrophobic surface after modifying 1-h-3-MIBr, which effectively prohibited moisture permeation. Halogen atoms have a great influence on passivation and hydrophobicity ability. Therefore, it is meaningful to choose a passivant containing suitable halogen, which would provide an insightful strategy for high-efficiency and stable perovskite devices.

Experiments

Materials

Dimethylformamide (DMF), dimethyl sulfoxide (DMSO), chlorobenzene (CB), isopropanol (IPA), 4-*tert*-butylpyridine (*t*-BP), acetonitrile, 2-propanol and bis(trifluoromethylsulfonyl) imidelithium salt (Li-TFSI) were purchased from Sigma-Aldrich. Tin (IV) oxide colloidal dispersion was purchased from Alfa Aesar. 1-h-3-MIHFP, 1-h-3-MICl, 1-h-3-MIBr were purchased from TCI. Methylammonium iodide (MAI), methylammonium chloride (MACl), Spiro-OMeTAD, FK209 Co(III) TFSI salt, lead(II) iodide (PbI_2, 99.99%) and formamidinium iodide (H2N = CHNH2I; FAI) were purchased from Xi'an Polymer Light Technology Corp. All materials were used as received without any further purification.

Device fabrication

The glass/FTO substrates were ultrasonically cleaned using deionized water, acetone, and IPA for 30 min, sequentially. The cleaned substrates were treated with O_2 plasma for 5 min, and then the SnO_2 colloidal solution (the volume ratio of SnO_2 colloidal precursor and water was 1 : 5) was spin-coated on the glass/FTO substrate at 3000 rpm for 30 s. The glass/FTO/SnO_2 samples were annealed at 150 °C for 30 min in the air. 1.5 mmol PbI_2 was dissolved in 1 mL mixed solution (DMF : DMSO = 9 : 1). 70 mg FAI, 3 mg MAI, and 7 mg MACl were dissolved in IPA. 50 μL PbI_2 solution was deposited by spin-coating at 2000 rpm for 30 s and then annealed at 80 °C for 1 min. 200 μL mixed IPA solution was deposited by spin-coating at 2000 rpm for 30 s. The thin films were annealed at 150 °C for 15 min in the air. After cooling to room temperature, surface modulator layers were deposited by spin-coating at 4000 rpm for 30 s using 2 mg mL^{-1} organic salts dissolved IPA. HTL solution was deposited by spin-coating at 3500 rpm for 30 s without further annealing. To obtain the HTL solution, 72.3 mg spiro-OMeTAD powder was dissolved in 1 mL CB with additives of 35 μL LiTFSI solution (260 mg mL^{-1} in acetonitrile) and 28.8 μL *t*-BP. Finally, 80 nm-thick Au was deposited using thermal evaporation.

Characterization

The *J*–*V* curves were measured using a xenon-lamp-based solar simulator (Newport, Class AAA Solar Simulator) with a source meter (Keithley B2902A Source Meter) under AM 1.5G illumination. The illumination was calibrated using an NREL-traceable KG5-filtered silicon reference cell. The scan speed was 0.1 V s^{-1}, and the scan delay time was 10 ms. All devices were attached with a metal mask with a circle-type aperture of 0.1 cm^2 to avoid light scattering from the metal electrode into the device during the measurement. The EQE was measured using a Crowntech QTest Station 2000ADI system. Steady-state PL (excitation at 532 nm) measurements were carried out on an Edinburgh Instruments Ltd (FLS980) instrument. TRPL spectra were collected using an Edinburgh Instruments (FLS980) fluorescence spectrometer with the time-correlated single-photon counting method. SEM images were recorded using a field emission scanning electron microscope (SU8020). The adsorption spectra were recorded using a PerkinElmer 10 UV-Lambda 950 instrument. The static water contact angles were measured using a contact angle meter (DSA100). XPS data were measured on a Thermo Fisher Scientific (K-Alpha system) instrument using Al Kα as the exciting X-ray source at a pressure of 1×10^{-8} Pa.

Results and discussion

The different surface modulator layers were fabricated by the spin-coating method, as shown in Fig. 1a. Fig. 1b–d give the molecular structures of various surface modulators. It is clear that the difference between surface modulators is the halide anions. The morphologies of perovskite films without and with surface modulator layers were studied by scanning electron microscopy (SEM). Fig. 1e–h shows the top-view SEM images of the pristine perovskite and modified perovskite films. It can be seen that the morphology does not change obviously when covered by chemisorbed capping layers.

Fig. 1i–l shows the water contact angles of the perovskite film without and with surface modulator layers. The same concentration (2 mg mL^{-1}) of the passivant was spun onto the perovskite film. The static water contact angles of control and optimized perovskite films were measured. The contact angle of the pristine perovskite film was 57.22°, and it dramatically increased to 81.55°, 83.67°, and 91.25° for the 1-h-3-MIHFP, 1-h-3-MICl, and 1-h-3-MIBr, respectively. The significantly increased contact angles are due to the hydrophobic organic moieties in surface modulators. The perovskite covered by 1-h-3-MIBr showed the largest water contact angle compared to other surface modulators, likely due to the stronger molecules symmetry caused by a larger ionic radius of Br. The large water contact angle would enhance the barrier for moisture permeation to improve the stability of perovskite.[35]

The perovskite film with 1-h-3-MIBr was selected as the representation, and positive secondary ion depth profiles were measured to investigate the distribution of the elements using a surface modulator. Fig. 2a and b show the time-of-flight secondary-ion mass spectrometry (TOF-SIMS) results of the perovskite without and with 1-h-3-MIBr deposited on FTO substrates. Fig. S1† shows the photos of the samples before and after sputter etching. Approximately, the positions of various ions can be detected by the depth profiles during the sputtering process. The traces for ions directly related to $FA_{0.95}MA_{0.05}PbI_3$ (Pb^+), FTO (Sn^+), and 1-h-3-MIBr (Br^+) when sputtering depth of the films. The trace of the Pb^+ position appears in the plateau part and then decreases with increasing sputtering time. The Pb^+ and Sn^+ positions are simultaneously observed, which suggests the ion migration into FTO from perovskite. It cannot detect the Br^+ position in pristine perovskite (Fig. 2a), and this position clearly identifies in perovskite with 1-h-3-MIBr (Fig. 2b). The signal of the Br^+ position quickly disappears with increasing sputtering time, indicating that1-h-3-MIBr forms an ultrathin film on perovskite. Fig. 2c, d, and f, g show the two-dimensional and three-dimensional depth profiles of Br elements for perovskite without and with 1-h-3-MIBr, respectively. For the pristine sample, negligible Br^+ was detected likely due to the cross-contamination during the fabrication/measurement process. For a sample of perovskite with 1 h-3MIBr, the Br elements are mostly focused on the perovskite surface. TOF-SIMS results revealed that the surface modulator forms a uniform thin film on the perovskite surface.

The optical and charge transfer of the perovskite covered by different surface modulator layers were measured. Fig. 3a shows the normalized absorption and photoluminescence (PL) spectra of perovskite without and with different surface modulator layers. It is clear that the absorb edges and PL peaks of the perovskite show a blue shift, which should be caused by the reduced defects by surface modulator layers,[36] as discussed below. Fig. 3b shows the steady-state PL spectra of the perovskite with and without surface modulators. All surface modulators could improve the peak intensity, and the perovskite with 1-h-3-MIBr gives the strongest PL intensity, demonstrating the fewest charge recombination.

The time-resolved PL (TRPL) measurements were tested to investigate the carrier transfer dynamics. Fig. 3c shows the TRPL spectra of the perovskite without and with surface modulator layers. The carrier decay lifetime (τ) can be fitted by an exponential equation.[37,38] As a result, the carrier decay lifetimes are 328.33 ns, 646.71 ns, 498.88 ns, and 1265.60 ns for pristine perovskite, perovskite with 1-h-3-MIHFP, 1-h-3-MICl, and 1-h-3-MIBr, respectively. The perovskite with 1-h-3-MIBr showed the longest carrier lifetime, indicating efficient charge carrier dissociation and suppressed non-radiative recombination.

The perovskite devices were fabricated to evaluate the influence of different surface modulators. The cross-sectional SEM image of the completed device is shown in Fig. S2.† FTO and Au have been used as the anode and cathode, respectively. SnO_2 and 2,2′,7,7′-tetrakis(*N*,*N*-di-*p*-methoxyphenylamine)-9,9′-spirobifluorene (spiro-OMeTAD) were employed as the electron transport layer (ETL) and hole transport layer (HTL), respectively. $FA_{0.95}MA_{0.05}PbI_3$ was adopted as an absorber, and different ionic organic modulators are developed as surface

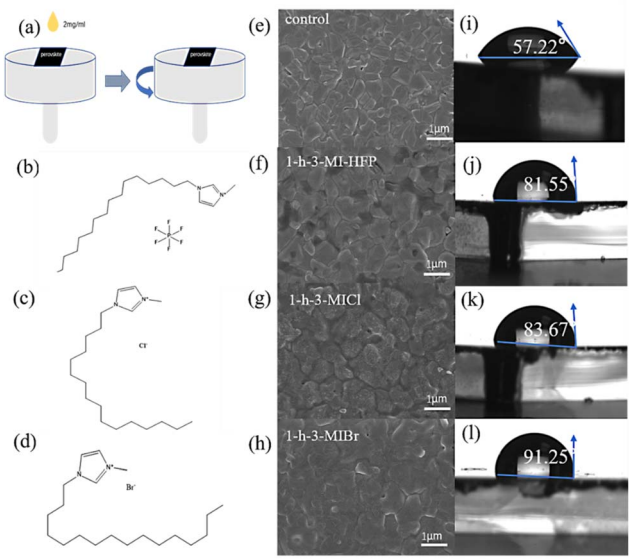

Fig. 1 (a) Preparation process of different surface modulator layers on the perovskite films. Molecular structures of (b) 1-h-3-MIHFP, (c) 1-h-3-MICl, and (d) 1-h-3-MIBr. (e) Top-view SEM images of perovskite films (e) without and with (f) 1-h-3-MIHFP, (g) 1-h-3-MICl, and (h) 1-h-3-MIBr. Water contact angles of (i) pristine perovskite film, and perovskite covered by (j) 1-h-3-MIHFP, (k) 1-h-3-MICl, and (l) 1-h-3-MIBr. The photos were taken at 5 s after dropping water on the film.

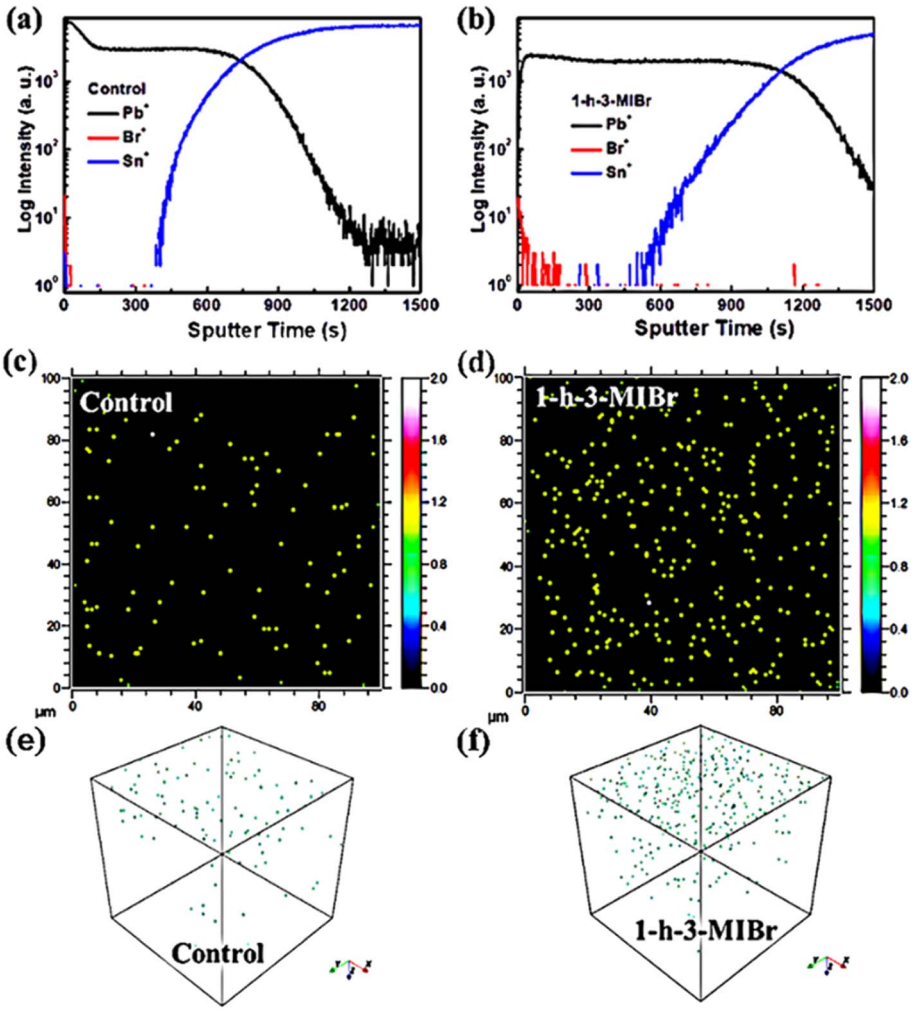

Fig. 2 TOF-SIMS results of (a) pristine perovskite and (b) perovskite with 1-h-3-MIBr deposited on FTO substrates. Two-dimensional depth profiles of Br elements for (c) pristine perovskite and (d) perovskite with 1-h-3-MIBr. Three-dimensional depth profiles analysis of Br distribution within (e) pristine perovskite and (f) perovskite with 1-h-3-MIBr.

modulator layers. Fig. 4a shows the current density–voltage (*J*–*V*) curves of PSCs without and with various surface modulator layers, and the key photovoltaic parameters including short-circuit current density (J_{sc}), open-circuit voltage (V_{oc}), fill factor (FF) and PCE are summarized in Table 1. The PCE of the best control perovskite device was 21.08% with J_{sc} of 25.67 mA cm^{-2}, V_{oc} of 1.08 V, and FF of 75.87%. When the perovskite is covered by surface modulators, both V_{oc} and FF are enhanced. The perovskite device with 1-h-3-MIBr exhibits the largest V_{oc} of 1.12 V and FF of 80.95%, yielding the highest efficiency of 23.32%. The high V_{oc} and FF are attributed to the long carrier lifetime (Fig. 3b and c) and the decreased carrier recombination (as discussed below) when using 1-h-3-MIBr surface modulator. In addition, the performance of our device with passivant has been compared with data from previous reports (Table S1†), and it is clear that our device shows high efficiency. Fig. 4b shows the external quantum efficiency (EQE) measurements of the perovskite devices without and with 1-h-3-MIBr. The integrated photocurrents are 24.41 mA cm^{-2} and 24.42 mA cm^{-2}, in agreement with *J*–*V* results.

In addition, 13 individual devices for each surface modulator layer have been fabricated and tested to accurately quantify the repeatability of the perovskite devices. The parameter distribution histograms are shown in Fig. S3,† and the statistics are listed in Tables S2–S5.† All the devices exhibit good repeatability with a small standard deviation, indicating that these ionic organic modulators are excellent surface modulators in the PSCs. The above results revealed that 1-h-3-MIBr is the most effective surface modulator, and the below discussions thereby focus on perovskite with 1-h-3-MIBr.

Environmental stability is a key characteristic of PSCs. Fig. 4c shows the long-term environmental stability of the perovskite devices without and with 1-h-3-MIBr. The PCE of the unencapsulated device with 1-h-3-MIBr maintains 75.42% of its initial efficiency under about 35% humidity stored in the air for 28 days. However, the efficiency of the control device without 1-h-3-MIBr only holds 44.49% of its initial value. The excellent environmental stability originates from the hydrophobic perovskite surface covered by 1-h-3-MIBr (Fig. 1l), which successfully blocks the moisture permeation into the device.

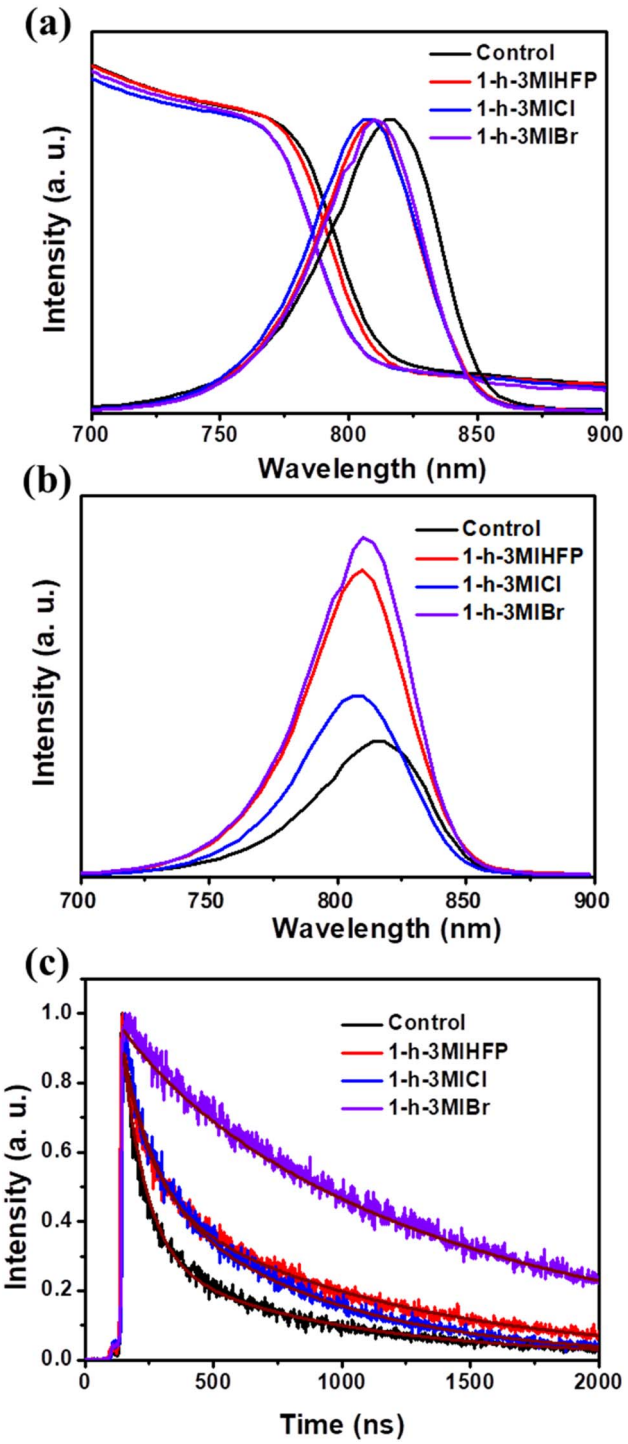

Fig. 3 (a) Absorption and PL spectra of the perovskite films without and with different surface modulator layers. These data are normalized, and the background has been corrected. (b) Steady-state PL and (c) TRPL spectra of the perovskite without and with various surface modulator layers.

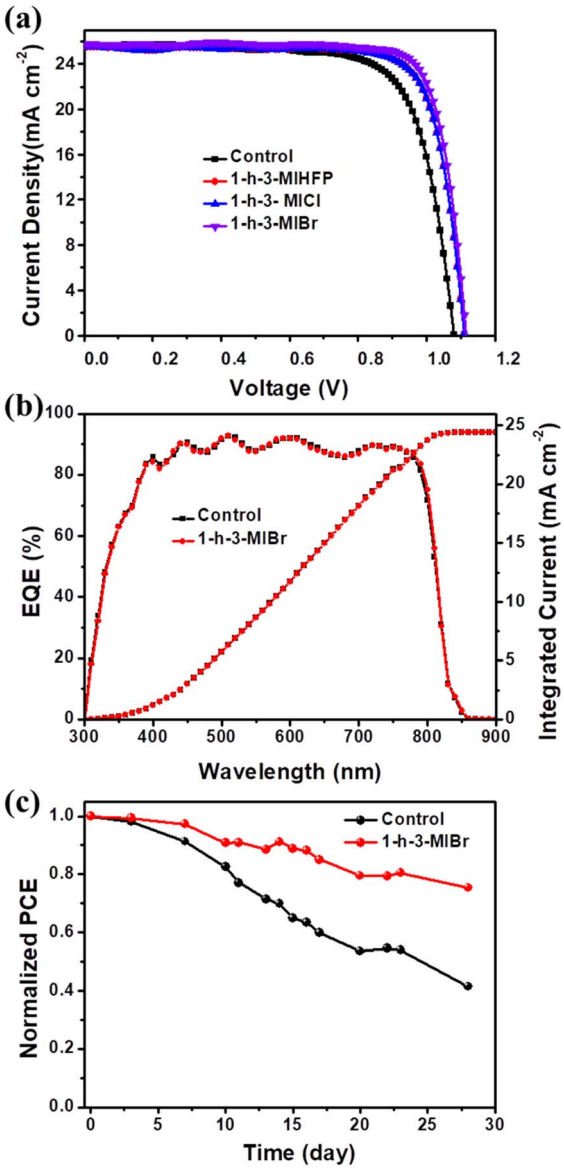

Fig. 4 (a) J–V curves of PSCs without and with different surface modulator layers. (b) EQE and integrated photocurrent of PSCs without and with 1-h-3-MIBr. (c) Long-term environmental stability of the unencapsulated PSCs without and with 1-h-3-MIBr under about 35% humidity stored in the air for 28 days.

Table 1 The key parameters of the best PSCs without and with different surface modulator layers

Device	V_{oc} (V)	J_{sc} (mA cm^{-2})	FF (%)	PCE (%)
Control	1.08	25.68	75.87	21.08
1-h-3-MIHFP	1.11	25.89	79.34	22.81
1-h-3-MICl	1.09	25.79	79.95	22.50
1-h-3-MIBr	1.12	25.84	80.95	23.32

Fig. 5a shows the ultraviolet photoelectron spectrometer (UPS) results of the perovskite without and with 1-h-3-MIBr. The Fermi level (E_F) is calculated by equation $E_F = E_{cut} - 21.22$ eV, where E_{cut} is the cut-off binding energy, and 21.22 eV is the emission energy of the helium irradiation. The E_{cut} of pristine perovskite and perovskite with 1-h-3-MIBr are 16.76 eV and 17.01 eV, respectively. Thus, the E_F of the pristine perovskite and perovskite with 1-h-3-MIBr are −4.46 eV and −4.21 eV,

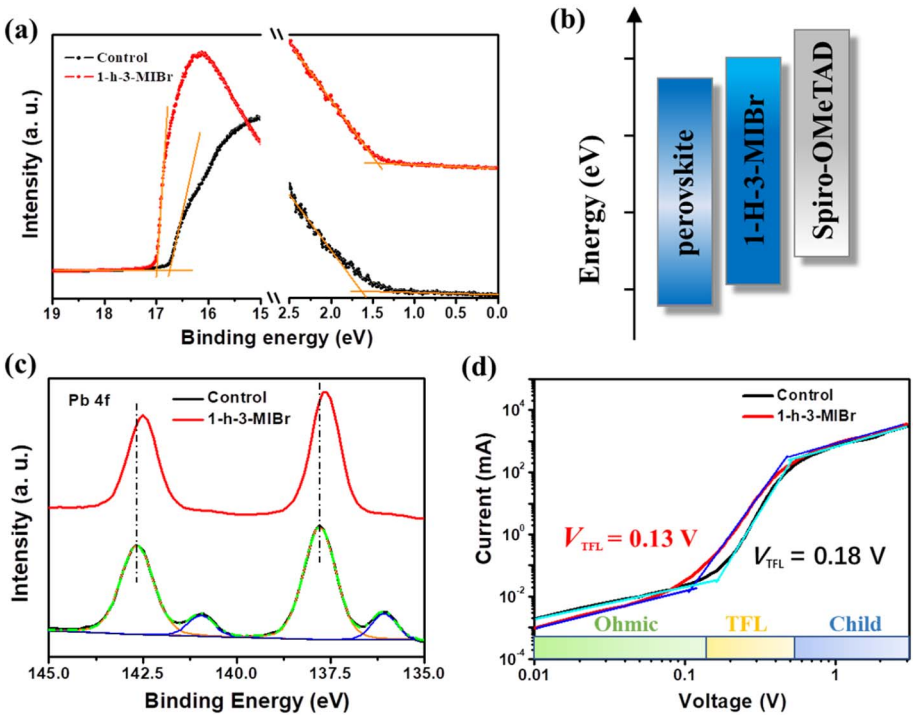

Fig. 5 (a) UPS analysis of different perovskite films. (b) Energy levels between different perovskite films and spiro-OMeTAD. (c) XPS core levels for Pb 4f in different perovskite films. (d) Dark *I*–*V* traces of the different perovskite films showing the ohmic, TFL, and child regions.

respectively. The Fermi edge (E_{edge}) of the pristine perovskite and perovskite with 1-h-3-MIBr are 1.62 eV and 1.44 eV (Fig. 5a), respectively. Therefore, the valence band (E_{VB}) of the pristine perovskite and the perovskite with 1-h-3-MIBr are −6.08 eV and −5.65 eV according to the equation of $E_{VB} = E_F - E_{edge}$. The energy–level diagram is described in Fig. 5b. The E_{VB} of perovskite based on 1-h-3-MIBr is closer to spiro-OMeTAD (HTL) than that of pristine perovskite, leading to larger V_{oc} due to less energy loss during charge transfer.[39]

X-ray photoelectron spectra (XPS) were collected to identify the interaction between the perovskite and 1-h-3-MIBr. Fig. 5c shows the XPS results of Pb 4f for the pristine perovskite and perovskite with 1-h-3-MIBr. The binding energy scale for XPS was calibrated according to the C 1 s line at 284.8 eV. There is a small binding energy at 141.0 eV, corresponding to the Pb 0 core level for the pristine perovskite. This binding energy disappears after covering 1-h-3-MIBr thin film. Meanwhile, the Pb 4f peaks of the perovskite with 1-h-3-MIBr shift to a lower binding energy compared to the pristine perovskite. These results indicate that the 1-h-3-MIBr reacts with uncoordinated Pb^{2+} ions, which would reduce the defects due to the decreased ion vacancy.

Fig. 5d shows the dark current–voltage (*I*–*V*) curves of the single carrier devices. The defect density (N_t) can be calculated by the equation of $N_t = 2\varepsilon_0\varepsilon_r V_{TFL}/eL^2$.[40] Where the ε_0 is the vacuum permittivity, ε_r is the relative dielectric constant of perovskite, e is the element charge, and *L* is the thickness of the perovskite film. The V_{TFL} is the trap-filled limit voltage, which can be obtained from the dark *I*–*V* curves. The V_{TFL} values are 0.13 V and 0.18 V for the pristine perovskite and perovskite with 1-h-3-MIBr, respectively. Therefore, the defect densities are 3.62×10^{14} and 2.58×10^{14} cm^3 for the control perovskite and perovskite with 1-h-3-MIBr, respectively. The defect density calculation results are in good agreement with the above analysis. The low defect density significantly decreases the charge recombination, resulting in high V_{oc} and FF.

Conclusion

In summary, we developed several ionic organic modulators including 1-h-3-MIHFP 1-h-3-MICl, and 1-h-3-MIBr as the surface modulator layers to modify the surface properties of the perovskite film. The perovskite device based on 1-h-3-MIBr exhibited the highest efficiency of 23.32% with improved V_{oc} and FF. The high performance is caused by the suitable energy level, enhanced carrier lifetime, and reduced defects, which lead to effective carrier transfer and decreased charge recombination. The 1-h-3-MIBr forms the uniform thin film on the perovskite to increase the surface hydrophobicity, which inhibits the moisture permeation, leading to the meaningfully improved long-term environmental stability of PSCs. This research provides an insightful strategy for the selection of post-treatment materials for high-efficiency and stable perovskite devices.

Conflicts of interest

There are no conflicts to declare.

Acknowledgements

The authors acknowledge support from the National Natural Science Foundation of China (Grant No. 61975106), the Strategic Priority Research Program of the Chinese Academy of Sciences (Grant No. XDA17040506), the National University Research Fund (Grant No. GK261001009), the Innovative Research Team (Grant No. IRT_14R33), the 111 Project (Grant No. B14041), and the Shaanxi Science and Technology Department (20201101012).

References

1 Q.-Q. Chu, B. Cheng and B. Fang, *Matter*, 2022, **5**, 2584–2586.
2 Q.-Q. Chu, B. Ding, Q. Qiu, Y. Liu, C.-X. Li, C.-J. Li, G.-J. Yang and B. Fang, *J. Mater. Chem. A*, 2018, **6**, 8271–8279.
3 X. Zheng, Y. Hou, C. Bao, J. Yin, F. Yuan, Z. Huang, K. Song, J. Liu, J. Troughton, N. Gasparini, C. Zhou, Y. Lin, D.-J. Xue, B. Chen, A. K. Johnston, N. Wei, M. N. Hedhili, M. Wei, A. Y. Alsalloum, P. Maity, B. Turedi, C. Yang, D. Baran, T. D. Anthopoulos, Y. Han, Z.-H. Lu, O. F. Mohammed, F. Gao, E. H. Sargent and O. M. Bakr, *Nat. Energy*, 2020, **5**, 131–140.
4 NREL, **www.nrel.gov/pv/cell-efficiency.html**.
5 A. Kojima, K. Teshima, Y. Shirai and T. Miyasaka, *J. Am. Chem. Soc.*, 2009, **131**, 6050–6051.
6 D. Yang, R. Yang, K. Wang, C. Wu, X. Zhu, J. Feng, X. Ren, G. Fang, S. Priya and S. Liu, *Nat. Commun.*, 2018, **9**, 3239.
7 J. Feng, X. Zhu, Z. Yang, X. Zhang, J. Niu, Z. Wang, S. Zuo, S. Priya, S. Liu and D. Yang, *Adv. Mater.*, 2018, **30**, 1801418.
8 K. Wang, X. Liu, R. Huang, C. Wu, D. Yang, X. Hu, X. Jiang, J. C. Duchamp, H. Dorn and S. Priya, *ACS Energy Lett.*, 2019, **4**, 1852–1861.
9 Z.-W. Gao, Y. Wang and W. C. H. Choy, *Adv. Energy Mater.*, 2022, **12**, 2104030.
10 Q.-Q. Chu, B. Cheng and B. Fang, *Matter*, 2022, **5**, 2444–2446.
11 M. Du, S. Zhao, L. Duan, Y. Cao, H. Wang, Y. Sun, L. Wang, X. Zhu, J. Feng, L. Liu, X. Jiang, Q. Dong, Y. Shi, K. Wang and S. Liu, *Joule*, 2022, **6**, 1931–1943.
12 X. Ren, D. Yang, Z. Yang, J. Feng, X. Zhu, J. Niu, Y. Liu, W. Zhao and S. F. Liu, *ACS Appl. Mater. Interfaces*, 2017, **9**, 2421–2429.
13 Y. Chen, X. Zuo, Y. He, F. Qian, S. Zuo, Y. Zhang, L. Liang, Z. Chen, K. Zhao, Z. Liu, J. Gou and S. Liu, *Advanced Science*, 2021, **8**, 2001466.
14 D. Yang, R. Yang, X. Ren, X. Zhu, Z. Yang, C. Li and S. Liu, *Adv. Mater.*, 2016, **28**, 5206–5213.
15 Z. Wu, E. Bi, C. Li, L. Chen, Z. Song and Y. Yan, *Sol. RRL*, 2023, **7**, 2200571.
16 S.-Y. Hsiao, H.-L. Lin, W.-H. Lee, W.-L. Tsai, K.-M. Chiang, W.-Y. Liao, C.-Z. Ren-Wu, C.-Y. Chen and H.-W. Lin, *Adv. Mater.*, 2016, **28**, 7013–7019.
17 H. Shen, Y. Wu, J. Peng, T. Duong, X. Fu, C. Barugkin, T. P. White, K. Weber and K. R. Catchpole, *ACS Appl. Mater. Interfaces*, 2017, **9**, 5974–5981.
18 F. Wang, P. Wai-Keung Fong, Z. Ren, H.-L. Xia, K. Zhou, K. Wang, J. Zhu, X. Huang, X.-Y. Liu, H. Wang, Y. Shi, H. Lin, Q. Zhu, G. Li and H. Hu, *J. Energy Chem.*, 2022, **73**, 599–606.
19 L. Fu, H. Li, L. Wang, R. Yin, B. Li and L. Yin, *Energy Environ. Sci.*, 2020, **13**, 4017–4056.
20 Y. Shao, Y. Fang, T. Li, Q. Wang, Q. Dong, Y. Deng, Y. Yuan, H. Wei, M. Wang, A. Gruverman, J. Shield and J. Huang, *Energy Environ. Sci.*, 2016, **9**, 1752–1759.
21 J. Chen and N.-G. Park, *Adv. Mater.*, 2019, **31**, 1803019.
22 Y. Yuan, T. Li, Q. Wang, J. Xing, A. Gruverman and J. Huang, *Sci. Adv.*, 2017, **3**, e1602164.
23 Z. Ni, C. Bao, Y. Liu, Q. Jiang, W.-Q. Wu, S. Chen, X. Dai, B. Chen, B. Hartweg, Z. Yu, Z. Holman and J. Huang, *Science*, 2020, **367**, 1352–1358.
24 J. Xia, C. Liang, H. Gu, S. Mei, S. Li, N. Zhang, S. Chen, Y. Cai and G. Xing, *Energy Environ. Mater.*, 2023, **6**, e12296.
25 G. Wu, R. Liang, M. Ge, G. Sun, Y. Zhang and G. Xing, *Adv. Mater.*, 2022, **34**, 2105635.
26 Z.-E. Shi, J.-Y. Long, C.-W. Li, S.-Y. Hsieh, Y.-S. Hsiao, C.-P. Chen and Y.-H. Yu, *Sustainable Energy Fuels*, 2022, **6**, 1950–1958.
27 S. Wang, Z. Ma, B. Liu, W. Wu, Y. Zhu, R. Ma and C. Wang, *Sol. RRL*, 2018, **2**, 1800034.
28 X. Ye, H. Cai, Q. Sun, T. Xu, J. Ni, J. Li and J. Zhang, *Org. Electron.*, 2022, **106**, 106542.
29 Y. Hu, Z. Zhang, A. Mei, Y. Jiang, X. Hou, Q. Wang, K. Du, Y. Rong, Y. Zhou, G. Xu and H. Han, *Adv. Mater.*, 2018, **30**, 1705786.
30 Y. Rakita, S. Gupta, D. Cahen and G. Hodes, *Chem. Mater.*, 2017, **29**, 8620–8629.
31 H. Cheng, Y. Li, G. Zhao, K. Zhao and Z.-S. Wang, *ACS Appl. Mater. Interfaces*, 2019, **11**, 28960–28967.
32 M. Zhong, L. Chai, Y. Wang and J. Di, *J. Alloys Compd.*, 2021, **864**, 158793.
33 R. Sandoval-Torrientes, J. Pascual, I. García-Benito, S. Collavini, I. Kosta, R. Tena-Zaera, N. Martín and J. L. Delgado, *ChenSusChem*, 2017, **10**, 2023–2029.
34 P. Chen, Y. Bai, S. Wang, M. Lyu, J.-H. Yun and L. Wang, *Adv. Funct. Mater.*, 2018, **28**, 1706923.
35 A. H. Proppe, M. Wei, B. Chen, R. Quintero-Bermudez, S. O. Kelley and E. H. Sargent, *J. Am. Chem. Soc.*, 2019, **141**, 14180–14189.
36 Q. Cai, Z. Lin, W. Zhang, X. Xu, H. Dong, S. Yuan, C. Liang and C. Mu, *J. Phys. Chem. Lett.*, 2022, **13**, 4598–4604.
37 E. V. Péan, S. Dimitrov, C. S. De Castro and M. L. Davies, *Phys. Chem. Chem. Phys.*, 2020, **22**, 28345–28358.
38 J. Feng, Z. Yang, D. Yang, X. Ren, X. Zhu, Z. Jin, W. Zi, Q. Wei and S. Liu, *Nano Energy*, 2017, **36**, 1–8.
39 M. Rai, L. H. Wong and L. Etgar, *J. Phys. Chem. Lett.*, 2020, **11**, 8189–8194.
40 N. Zhou, Y. Shen, Y. Zhang, Z. Xu, G. Zheng, L. Li, Q. Chen and H. Zhou, *Small*, 2017, **13**, 1700484.